Journal of Vibration Engineering & Technologies (2024) 12:6527–6547
https://doi.org/10.1007/s42417-023-01268-x

ORIGINAL PAPER

Analysis of Natural Frequencies in Non-uniform Cross-section Functionally Graded Porous Beams

Vyacheslav N. Burlayenko[1] · **Reijo Kouhia**[2]

Received: 11 July 2023 / Revised: 16 October 2023 / Accepted: 19 December 2023 / Published online: 13 February 2024

Abstract

Purpose The study aims to analyze the free vibration behavior of functionally graded porous beams with non-uniform rectangular cross-sections, investigating four distinct porosity distribution across the beam's thickness.

Methods Utilizing the Euler–Bernoulli beam model and Hamilton's principle, the equation of motion is derived. Four different boundary conditions (clamped–clamped, clamped-free, clamped–pinned, and pinned–pinned) are considered, and the resulting equation is solved using the differential transform method. Verification of accuracy is ensured through comparison with solutions for natural frequencies found in existing literature.

Results and Conclusion The study provides validated natural frequency solutions for functionally graded porous beams with non-uniform rectangular cross-sections, confirming the accuracy of the proposed method through literature comparison. A comprehensive parametric study reveals significant insights into the influence of various factors on natural frequencies, including porosity volume fractions, types of porosity distribution, taper ratios, and boundary conditions. These findings deepen our understanding of free vibration analysis for functionally graded porous beams, offering valuable guidance for engineering design and structural optimization in relevant applications.

Keywords Natural frequencies · Functionally graded porous beam · Non-uniform cross-section · Differential transform method

Introduction

The concept of functionally graded materials (FGMs) originated in the field of engineering, where materials with continuously varying composition or microstructure were developed to optimize their mechanical, thermal, electrical and other properties. Functionally graded porous materials (FGPMs), such as metal foams, take this idea further by incorporating porosity as an additional design parameter.

FGPMs offer a series of advantages over homogeneous materials or composite materials with a layered structure. The void spaces created by the pores reduce the material's density, resulting in a lighter structure. This characteristic is particularly worthwhile in industries such as aerospace and automotive, where weight reduction is a critical factor. Moreover, by controlling the distribution of porosity, it is possible to achieve specific combinations of properties, such as mechanical strength, thermal conductivity, or fluid permeability, within a single material [1]. In addition, the spatial variation of properties allows FGPMs to avoid discontinuities in temperature and stress distributions as a result delamination issues inherent to simple layered configurations, e.g., in Refs. [2–5] to name a few, can be eliminated [6].

On the other hand, the manufacturing methods employed in the production of FGM beams and panels inevitably result in the formation of pores within the material volume [7]. The presence of pores can introduce certain challenges and drawbacks to the FGM. One significant concern is the potential compromise in structural integrity. Pores weaken the material and reduce its load-bearing capacity, making it more susceptible to failure under stress or external forces. Moreover, pores affect the elastic and mechanical properties of the

✉ Vyacheslav N. Burlayenko
viacheslav.burlaienko@khpi.edu.ua; burlayenko@yahoo.com

Reijo Kouhia
reijo.kouhia@tuni.fi

1 Department of Applied Mathematics, National Technical University 'KhPI', 2 Kyrpychova Str., Kharkiv 61002, Ukraine

2 Faculty of Built Environment, Tampere University, POB 600, 33101 Tampere, Finland

material changing structural responses of the FGM beams and panels. As a result, research focused on studying the mechanical behavior and dynamic characteristics of FGM structures with porosity is of great significance. Herewith, the accurate prediction of natural frequencies is crucial for vibration control of such objects.

The literature search revealed an extensive studies discussing the dynamic behavior of FGM beams and panels with and without porosities. Vibrations in perfect FGM beams, plates, and shells have been examined using classical and various shear deformation theories [8, 9]. Those analyses involved equivalent single-layer (ESL) models [10, 11], layer-wise (LW) descriptions [12, 13], and the three-dimensional approach [14–16]. Different methodologies have been employed, ranging from analytical techniques to numerical simulations, e.g., in Refs. [17–21] among the latest. However, it is crucial to investigate the influence of porosity since it serves as a vital parameter in the design of modern structures.

Inspired by recent advancements in FG porous engineering materials, a significant number of researchers have undertaken studies on the dynamics of FGP beams [22–26], and plates and shells [27–29]. In these studies, while analyzing the vibration response of FG porous structures, the analysts have made adjustments to the aforementioned theories and methodologies, originally developed for ideal FGM beams, plates, and shells in order to incorporate graded porosities. Those porosities can exhibit uniform or non-uniform symmetric/non-symmetric distributions throughout the thickness of the structures.

Inhomogeneous structures with variable cross-sections are extensively utilized in diverse engineering applications, including helicopter rotor blades, wind turbines, ship propellers, and space and marine structures. These structures are favored for their ability to meet specific architectural requirements while achieving optimized weight and strength distribution. A variety of methods have been employed to solve the differential equations of motion for variable thickness FGM beams. In Ref. [30], the authors employed the dynamic stiffness method to analyze the dynamics of homogeneous tapered Euler–Bernoulli beams. In addition, in Ref. [31], the free vibrations of axially functionally graded (AFG) tapered Euler–Bernoulli beams were studied using the differential transformation and differential quadrature methods. The natural frequencies of the AFG Euler–Bernoulli beam with non-uniform cross-section were also investigated in Ref. [32] through the differential transformation method (DTM). Furthermore, the spline finite point method was utilized in Ref.[33] for the analysis of free transverse vibration of AFG tapered Euler–Bernoulli beams. The authors in Ref. [34] employed the asymptotic development method to study the free vibration of non-uniform AFG Euler–Bernoulli beams. A new hybrid approach based on the combination of the power series expansions and the Rayleigh–Ritz method for stability and free vibration analyses of AFG non-uniform beams supported by a constant Winkler–Pasternak elastic foundation was presented in Ref. [35]. A precise solution for free vibration of FG beams with variable cross-section resting on a Pasternak foundation was proposed in Ref. [36] using the separate variable method and Laplace transform within the framework of 2-D elastic theory. Furthermore, the vibrational characteristics of AFG tapered beams based on both Euler–Bernoulli and Timoshenko theories were analyzed in Ref. [37] utilizing the variational iteration method. In Ref. [38], the weighted residual collocation method with exact solution shape functions for the uniform beam as trial functions was employed to investigate the free transverse vibrations of variable cross-section cantilever FG beams with nonlinear profiles. In addition, the dynamic characteristics of an internal flexible FGM Euler–Bernoulli tapered microbeam were studied in Ref. [39] based on the modified couple stress theory.

The literature search revealed that there is a limited number of research regarding the vibration response of non-uniform cross-section FG porous beams, in comparison to the extensive studies available on vibrations of constant thickness porous beams. For instance, in Ref. [40], the authors have investigated the free vibration

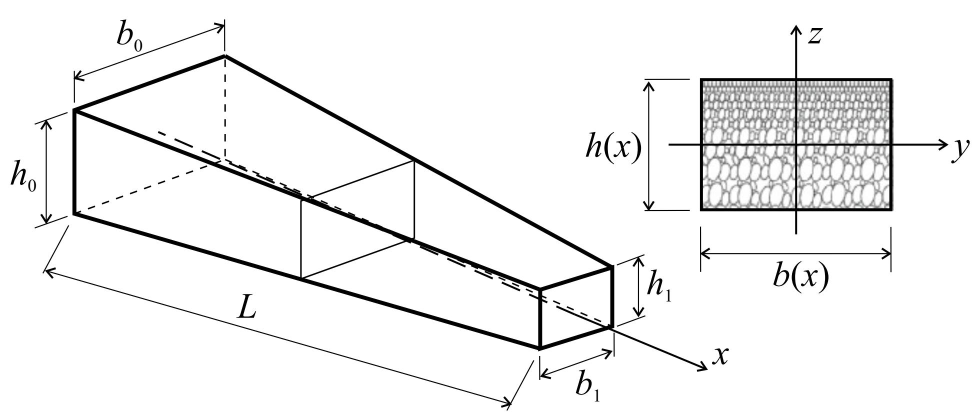

Fig. 1 Schematic of a non-uniform FGP beam

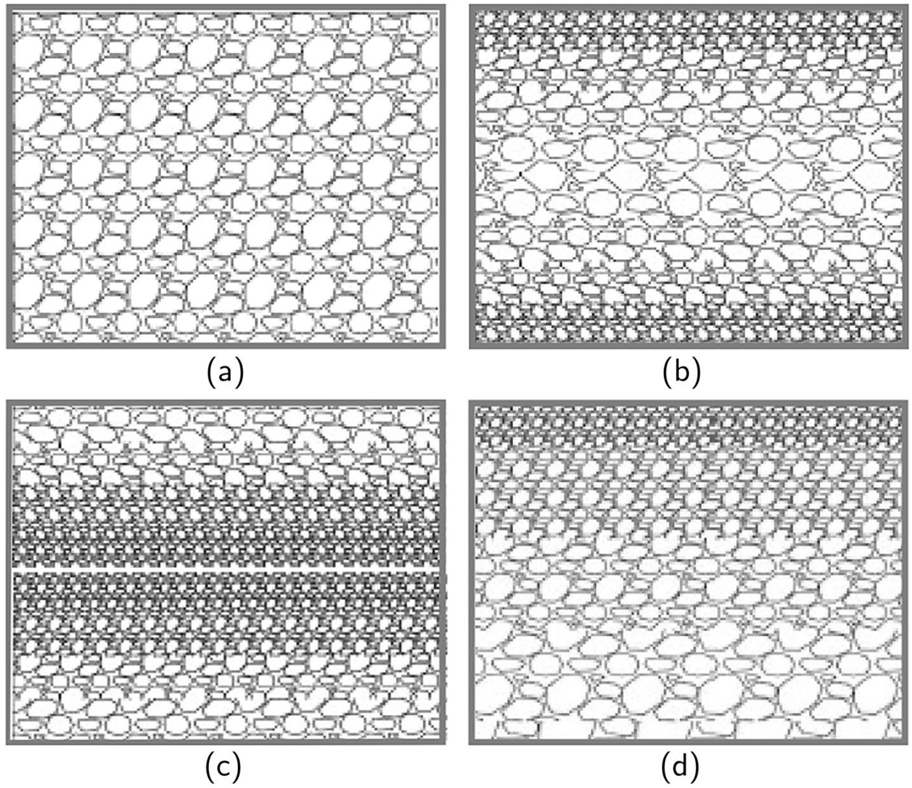

Fig. 2 Different porosity profiles of the FGP beam's cross-section

characteristics of a rotating double-tapered FG porous beam using the DTM. However, their analysis primarily focused on specific boundary conditions, tapering profiles, and porosity levels, leaving space for further exploration in this field. In the other work of the same authors [41], the DTM has been employed to examine the thermo-mechanical vibration behavior of non-uniform FG porous Euler–Bernoulli beams under a variety of thermal loadings. Furthermore, in Ref. [42], a finite-element dynamic analysis was conducted to examine the response of non-uniform FG porous beams subjected to multiple moving forces, employing the Timoshenko beam theory. In addition, in Ref. [43], the authors investigated the free vibration behavior of rotating FGM beams, including porosities with even or uneven distributions, using a modified variational method. The method utilized the Chebyshev series expansion and incorporated the fully geometrically nonlinear beam theory with Coriolis effect. In Refs. [44, 45], a novel approach based on spatial state equations and the associated state transition matrix has been proposed to compute the natural frequencies and mode shapes of Euler–Bernoulli and Timoshenko beams with arbitrary variations in material and geometrical properties, as well as discontinuities within the beams. Recently, in Refs. [46, 47], the discrete singular convolution method has been utilized to analyze the dynamic characteristics and buckling of non-uniform, multi-span, functionally graded graphene foam-reinforced beams under elastic boundary conditions.

This paper focuses on the free vibration analysis of non-uniform rectangular cross-section porous FG beams with four different porosity distributions. These porosity distributions, namely even and uneven with symmetric and non-symmetric profiles, are assumed to vary through the beam's thickness direction based on the modified Gibson–Ashby model [48]. The vibration response is analyzed using the Euler–Bernoulli beam theory. The equation of motion and natural boundary conditions are derived using Hamilton's principle. These equations in conjunction with four different beam edges' constraints such as pinned–pinned (P–P), clamped–clamped (C–C), clamped–pinned (C–P) and clamped-free (C-F) are solved using a semi-analytical DTM approach. Semi-analytical solutions of the natural frequencies are compared with existing results in the literature to validate the proposed technique and to ensure the accuracy and reliability of the approach. In addition, for the first time, a comprehensive parametric study is conducted to examine the influence of porosity volume fractions, types of porosity distribution, taper ratios, and boundary conditions on the natural frequencies of FG porous beams. The obtained results can serve as valuable references for validating other approaches and approximate methods, as well as providing insights to enhance the dynamic performance of FG porous beams.

Non-uniform FGP Beams

An FG porous beam with variable rectangular cross-section is schematically illustrated in Fig. 1. The beam has a length L and its cross-section parameters are width b and thickness h. The axis x indicates the beam length direction, while the axes y and z denote the directions of the beam's width and thickness, respectively.

The cross-section variations are assumed to exhibit symmetry about the mid-line ($z = 0$) of the beam. The width and thickness of the beam as functions of x can be written as

$$\begin{aligned} b(x) &= b_0\left(1 - c_b\frac{x}{L}\right)^m, \\ h(x) &= h_0\left(1 - c_h\frac{x}{L}\right)^n, \end{aligned} \tag{1}$$

where $c_b = 1 - \frac{b_1}{b_0}$ and $c_h = 1 - \frac{h_1}{h_0}$ are the width and height taper ratios, respectively. It is worth to mention that if $c_b = c_h = 0$, the beam would be uniform; if $c_b \neq 0$ and $c_h = 0$, the beam would be tapered with width but has a constant height; if $c_b = 0$ and $c_h \neq 0$, the beam would be tapered with height but has a constant width; and if $c_b \neq 0$ and $c_h \neq 0$, the beam would be double tapered. The power coefficients m and n allow for accounting for arbitrary variation of the geometrical parameters along the beam's length. Herewith, the rectangular cross-sectional area $A(x)$ and the second moment of inertia $I(x)$ vary along the beam's length as follows:

$$\begin{aligned} A(x) &= A_0\left(1 - c_b\frac{x}{L}\right)^m\left(1 - c_h\frac{x}{L}\right)^n, \\ I(x) &= I_0\left(1 - c_b\frac{x}{L}\right)^m\left(1 - c_h\frac{x}{L}\right)^{3n}, \end{aligned} \tag{2}$$

where A_0 and I_0 represent the area and second moment of inertia of the rectangular cross-section at $x = 0$, respectively.

Porosity changes the material properties of the beam, specifically, Young's modulus E and mass density ρ. This is similar to material profiles observed in perfect functionally graded materials. Here, we assume that the material properties vary continuously across the beam thickness, that is, they are functions of z. Four types of porosity distribution profiles such as even (type I) and uneven symmetric with stiffer layers in surface areas (type II), symmetric with a stiffer layer in the central area (type III), and non-symmetric (type IV) are considered, as shown in Fig. 2. These porosity distributions along the height h of the beam's cross-section at a given position on the x-axis can be defined as follows [23]:

$$\begin{aligned} E(z) &= E_0(1 - e_0\alpha), \\ \rho(z) &= \rho_0\sqrt{1 - e_0\alpha}, \end{aligned} \tag{3}$$

for type I profile, in which $\alpha = \frac{1}{e_0} - \frac{1}{e_0}\left(\frac{2}{\pi}\sqrt{1 - e_0} - \frac{2}{\pi} + 1\right)^2$,

$$\begin{aligned} E(z) &= E_0\left(1 - e_0\cos\left(\frac{\pi}{h}z\right)\right), \\ \rho(z) &= \rho_0\left(1 - e_m\cos\left(\frac{\pi}{h}z\right)\right), \end{aligned} \tag{4}$$

for type II profile,

$$\begin{aligned} E(z) &= E_0\left(1 - e_0\cos\left(\left|\frac{\pi}{h}z\right| - \frac{\pi}{2}\right)\right), \\ \rho(z) &= \rho_0\left(1 - e_m\cos\left(\left|\frac{\pi}{h}z\right| - \frac{\pi}{2}\right)\right), \end{aligned} \tag{5}$$

for type III profile, and

$$\begin{aligned} E(z) &= E_0\left(1 - e_0\cos\left(\frac{\pi}{2h}z + \frac{\pi}{4}\right)\right), \\ \rho(z) &= \rho_0\left(1 - e_m\cos\left(\frac{\pi}{2h}z + \frac{\pi}{4}\right)\right), \end{aligned} \tag{6}$$

for type IV profile.

In (3)–(6), we denote $e_0 = 1 - E_1/E_0$, $(0 < e_0 < 1)$ and $e_m = 1 - \rho_1/\rho_0$, $(0 < e_m < 1)$, where E_1 and E_0 are minimum and maximum values of Young's modulus, respectively, and also ρ_1 and ρ_0 are minimum and maximum values of mass density, respectively. Moreover, in the case of open-cell porous materials [48], the relationship between e_0 and e_m can be expressed in the form $e_m = 1 - \sqrt{1 - e_0}$.

It should be mentioned that the Poisson's ratio ν is assumed constant for all the types of porosity distributions.

Governing Equation of Motion

The inhomogeneous beam of length L is characterized by material properties that continuously vary in the through-thickness direction z, while the rectangular cross-section of the beam varies along the axial coordinate x. Transverse vibration of the beam takes place in the xz-plane. Let us consider the Euler–Bernoulli theory, which takes into account only the transverse displacement $\tilde{w}(x, z, t)$ and the curvature of the mid-line. Then, the displacements along the x- and z-axes are expressed in the form:

$$\begin{aligned} \tilde{u}(x, y, t) &= -z\frac{\partial w(x, t)}{\partial x}, \\ \tilde{w}(x, z, t) &= w(x, t). \end{aligned} \tag{7}$$

Based on the displacement field (7), only the normal strain component occurs as

$$\varepsilon_{xx} = -z\frac{\partial^2 w(x, t)}{\partial x^2}. \tag{8}$$

The corresponding normal stress can be obtained using one-dimensional Hooke's law as

$$\sigma_{xx} = E(z)\epsilon_{xx}. \tag{9}$$

Within this assumption, the strain and kinetic energies are defined, accordingly, as follows:

$$\begin{aligned} U &= \frac{1}{2}\int_0^L D_{11}(x)\left(\frac{\partial^2 w}{\partial x^2}\right)^2 dx, \\ K &= \frac{1}{2}\int_0^L m(x)\left(\frac{\partial w}{\partial t}\right)^2 dx. \end{aligned} \tag{10}$$

Herein, appropriate stiffness and inertia coefficients in (10) are computed, respectively, as

$$\begin{aligned} D_{11}(x) &= \int_{A(x)} z^2 E(z) dA, \\ m(x) &= \int_{A(x)} \rho(z) dA. \end{aligned} \tag{11}$$

Using Hamilton's principle $\delta\Pi = \delta\{\int_{t_1}^{t_2}(U-K)dt\} = 0$ with the virtual strain (δU) and kinetic (δK) energies, we can write the governing equation of motion of the FGP beam as

$$\frac{\partial^2}{\partial x^2}\left[D_{11}(x)\frac{\partial^2 w}{\partial x^2}\right] + m(x)\frac{\partial^2 w}{\partial t^2} = 0,\ 0 \le x \le L, \tag{12}$$

with natural boundary conditions and an initial condition as follows:

$$\begin{aligned} \frac{\partial}{\partial x}\left(D_{11}(x)\frac{\partial^2 w}{\partial x^2}\right)\Bigg|_0^L &= 0, \\ D_{11}(x)\frac{\partial^2 w}{\partial x^2}\Bigg|_0^L &= 0, \\ m(x)\frac{\partial w}{\partial x}\Bigg|_{t_1}^{t_2} &= 0. \end{aligned} \tag{13}$$

For harmonic vibration with frequency ω, the dynamic displacement field is defined by

$$w(x,t) = \bar{w}(x)(e)^{i\omega t}. \tag{14}$$

Substituting (14) into (12), it gives us an ordinary differential equation describing free transverse vibration of a non-uniform cross-section FG porous beam:

$$\frac{d^2}{dx^2}\left[D_{11}(x)\frac{d^2\bar{w}(x)}{x^2}\right] - m(x)\omega^2\bar{w} = 0,\ 0 \le x \le L. \tag{15}$$

Herewith, the stiffness $D_{11}(x)$ and inertia $m(x)$ coefficients can be expressed in the form:

$$\begin{aligned} D_{11}(x) &= E_z(x)I(x), \\ m(x) &= \rho_z(x)A(x), \end{aligned} \tag{16}$$

where the averaged Young's modulus $E_z(x)$ and mass density $\rho_z(x)$ are computed by analytical integration of (11) over the rectangular domain $A(x)$ for each type of porosity profile (3)–(6). The explicit forms of these expressions can be found in Appendix A.

Differential Transform Method

From a mathematical perspective, integrating Eq. (15) presents complexity due to variable coefficients arising from coordinate-dependent material properties and cross-sections. As a result, closed-form solutions are feasible only for specific cross-sectional shapes, porosity profiles, and boundary conditions. In this context, numerical methods like the finite-element method (FEM) are more effective, as they offer the necessary versatility to explore various geometric configurations and material characteristics However, the differential transform method can also be effectively employed for this purpose. In contrast to the traditional FEM, the DTM stands out for its accessibility, simplicity, and avoidance of finite-element meshes. As a semi-analytical method, it is inherently symbolic and eliminates the need for auxiliary parameters, assumed functions, or specific initial/boundary conditions when seeking the solution, unlike the approximations used in FEM. In addition, the DTM provides a series expansion solution for differential equations, enabling deeper insights into the system's behavior, whereas the FEM typically delivers numerical solutions without analytical expressions.

The DTM was initially introduced by G. E. Pukhov in 1978 [49], and the fundamental aspects of this method can be found in his original publications [50–52]. A recent comprehensive discussion on the status of the DTM, including its basics, drawbacks and limitations has been presented in Refs. [53, 54] and the references therein. An investigation into the convergence issues associated with DTM solutions has been reported in Refs. [32, 55]. Researchers, e.g., [56–58], have also explored innovative strategies to mitigate the limitations, combining the DTM with other techniques that provide accurate results in regions where the series solution may not suffice.

Besides the variety of the tasks to which the DTM can be applied, its accuracy and simplicity in calculating the natural frequencies makes it superior among many other semi-analytical methods mentioned in Introduction. The application of the DTM to address the free vibration problem of non-uniform inhomogeneous beams is reported in Refs. [31, 32, 40, 41] to name a few.

Following Ref. [32], we reformulate (15) in a form more suitable for its application in addressing the vibration problem using the DTM

$$\frac{d^4\bar{w}}{dx^4} + \bar{D}_1(x)\frac{d^3\bar{w}}{dx^3} + \bar{D}_2(x)\frac{d^2\bar{w}}{dx^2} - \omega^2\bar{M}(x)\bar{w} = 0, \tag{17}$$

where the variable coefficients will be denoted as $\bar{D}_1(x) = 2D'_{11}(x)/D_{11}(x)$, $\bar{D}_2(x) = D''_{11}(x)/D_{11}(x)$ and $\bar{M}(x) = m(x)/D_{11}(x)$. Here, and in what follows, the prime denotes a derivative with respect to the x-coordinate.

It's worth noting that the variable coefficients in (17) account for changes in both thickness and length directions. As a result, they exhibit a more complex structure in terms of the variable x, compared to the coefficients associated with functionally graded material properties that vary solely in the axial direction [30–32]. This complexity significantly slows down the computation and convergence rate of the DTM. To overcome this issue, the division operation in the domain of differential transformations is employed for the coefficients $\bar{D}_1(x)$, $\bar{D}_2(x)$ and $\bar{M}(x)$ before computing their appropriate images (discretes) [52].

Thus, by utilizing the domain of differential transformation, the solution of equation (17) at a certain point x_0 of the interval $0 \le x \le L$ can be represented as a set of recurrent algebraic equations [32]:

$$\begin{aligned} W(k+4) = \frac{k!}{(k+4)!}\Bigg\{ & \omega^2 \sum_{p=0}^{k} W(p)M(k-p) - \\ & \sum_{p=0}^{k} \frac{(p+3)!}{p!} W(p+3)D_1(k-p) \\ & - \sum_{p=0}^{k} \frac{(p+2)!}{p!} W(p+2)D_2(k-p) \Bigg\}, \end{aligned} \tag{18}$$

Table 1 Non-dimensional natural frequencies $\bar{\omega}_n$ of a double-tapered homogeneous beams with the height and width varying linearly along the beam length for different boundary constraints

C–F						C–C			P–P		
α	Mode	[30]	[33]	Present	Δ,%	[33]	Present	Δ,%	[33]	Present	Δ,%
0.1	1	3.67370	–	3.67370	0.0000	–	–	–	–	–	–
	2	21.5503	–	21.55025	0.0002	–	–	–	–	–	–
	3	59.1886	–	59.18864	0.0001	–	–	–	–	–	–
0.2	1	3.85511	3.8551	3.85512	0.0003	20.0968	20.09663	0.0008	8.8246	8.82458	0.0002
	2	21.0568	21.0569	21.05675	0.0002	55.3683	55.36495	0.0061	35.4665	35.46564	0.0024
	3	56.6303	56.6335	56.63035	0.0001	108.5357	108.51043	0.0233	79.7721	79.76244	0.0121
0.3	1	4.06694	–	4.06693	0.0002	–	–	–	–	–	–
	2	20.5555	–	20.55551	0.0000	–	–	–	–	–	–
	3	54.0152	–	54.01519	0.0000	–	–	–	–	–	–
0.4	1	4.31878	4.31878	4.31878	0.0000	17.7203	17.71987	0.0024	7.6314	7.63138	0.0003
	2	20.0500	20.0501	20.04998	0.0001	48.7027	48.69836	0.0089	31.2881	31.28711	0.0032
	3	51.3346	51.3378	51.33463	0.0001	95.3717	95.34452	0.0285	70.2453	70.23554	0.0139
0.5	1	4.62515	–	4.62515	0.0000	–	–	–	–	–	–
	2	19.5476	–	19.54761	0.0001	–	–	–	–	–	–
	3	48.5789	–	48.57890	0.0000	–	–	–	–	–	–
0.6	1	5.00904	5.00904	5.00903	0.0002	15.1914	15.18977	0.0107	6.2087	6.20862	0.0013
	2	19.0649	19.0651	19.06486	0.0002	41.4862	41.47654	0.0233	26.8534	26.85179	0.0060
	3	45.7384	45.7417	45.73837	0.0001	81.0196	80.97752	0.0519	60.0036	59.99137	0.0204
0.7	1	5.50926	–	5.50927	0.0002	–	–	–	–	–	–
	2	18.6412	–	18.64124	0.0002	–	–	–	–	–	–
	3	42.8104	–	42.81086	0.0011	–	–	–	–	–	–
0.8	1	6.19639	6.19639	6.19780	0.0228	12.3970	12.38438	0.1018	4.3536	4.37116	0.4033
	2	18.3855	18.3858	18.39428	0.0478	33.2794	33.21227	0.2017	21.9447	21.91152	0.1512
	3	39.8336	39.8376	39.86815	0.0867	64.5189	64.37748	0.2192	48.4357	48.46315	0.0567
0.9	1	7.20488	–	7.23501	0.4182	–	–	–	–	–	–
	2	18.6803	–	18.84108	0.8607	–	–	–	–	–	–
	3	37.1241	–	38.18606	2.8606	–	–	–	–	–	–

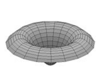

where $W(k)$, and $D_1(k)$, $D_2(k)$ and $M(k)$ are the images of the unknown amplitude $\bar{w}(x)$ and the given functions $\bar{D}_1(x)$, $\bar{D}_2(x)$ and $\bar{M}(x)$, respectively.

It is obvious that each recurrent equation in the system 18 is derived by sequentially varying the index k. However, the images $W(0)$, $W(1)$, $W(2)$, and $W(3)$ are not directly obtained from 18 as observed. Therefore, we can simplify this expression to the following form:

$$W(k+4) = B_k W(0) + C_k W(1) + G_k W(2) + H_k W(3), \tag{19}$$

where the explicit forms of the recurrent coefficients in (19) can be found in Ref. [32].

Once the spectrum $W(k)$ for chosen number of images is obtained, the original function $\bar{w}(x)$ is reconstructed as

$$\bar{w}(x,\omega) = W(0) + W(1)(x-x_0) + W(2)(x-x_0)^2 + W(3)(x-x_0)^3 + W(4)(x-x_0)^4 + \cdots + W(k)(x-x_0)^k. \tag{20}$$

Given that the images $W(k)$ at $k \geqslant 4$ depends on $W(0)$, $W(1)$, $W(2)$ and $W(3)$, Eq. (20) takes the form:

$$\bar{w}(x,\omega) = \left\{1 + \sum_{p=0}^{k-4} B_p (x-x_0)^{p+4}\right\} W(0) + \left\{(x-x_0) + \sum_{p=0}^{k-4} C_p (x-x_0)^{p+4}\right\} W(1) + \left\{(x-x_0)^2 + \sum_{p=0}^{k-4} G_p (x-x_0)^{p+4}\right\} W(2) + \left\{(x-x_0)^3 + \sum_{p=0}^{k-4} G_p (x-x_0)^{p+4}\right\} W(3). \tag{21}$$

By satisfying boundary conditions imposed on the beam ends in terms of transverse displacement $\bar{w}$, rotation angle θ, bending moment M and shear force Q, such that

$$\theta = \frac{d\bar{w}}{dx},\ M = -D_{11}(x)\frac{d^2\bar{w}}{dx^2} \text{ and } Q = -\frac{d}{dx}\left[D_{11}(x)\frac{d^2\bar{w}}{dx^2}\right]$$

we arrive at the eigenvalue problem for each case of constraints in the following form [32]:

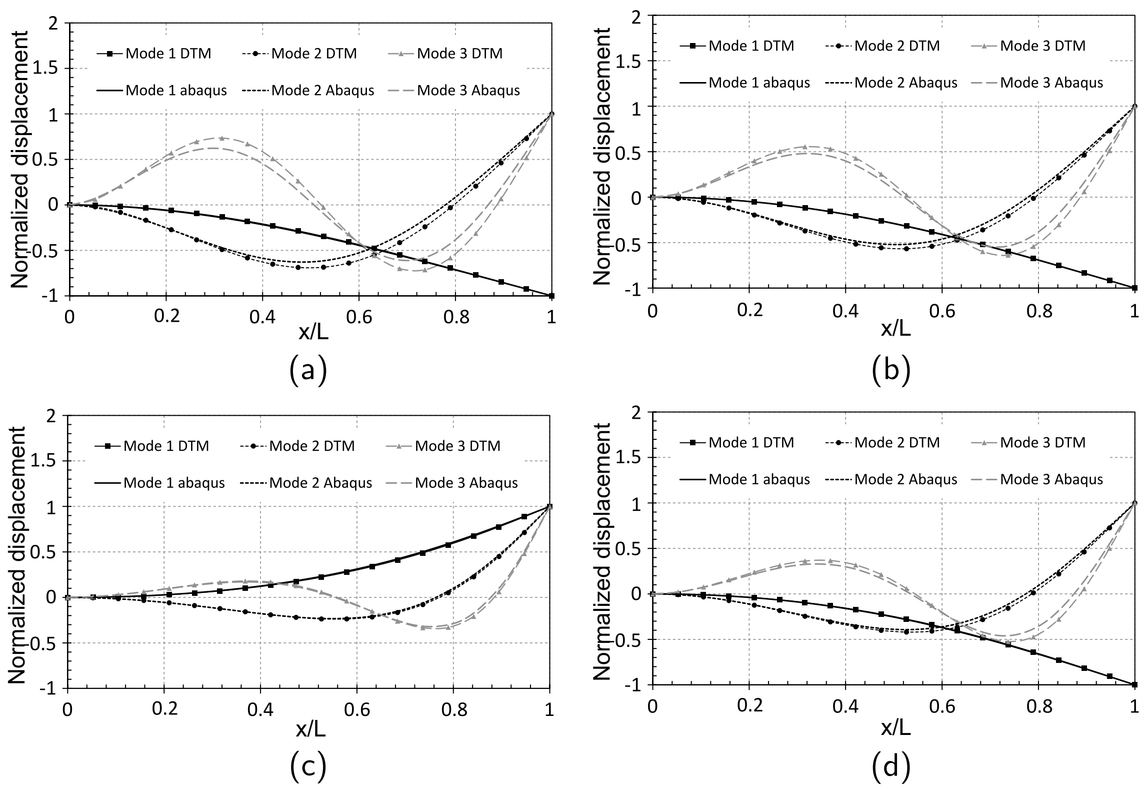

Fig. 3 The mode shapes associated with the first three natural frequencies for the cantilever double-tapered homogeneous beam for different taper ratios: (a) α=0.2; (b) α=0.4; (c) α=0.6; and (d) α=0.8

Table 2 Non-dimensional natural frequencies $\bar{\omega}_n$ of an AFGM double-tapered beams with both height and width varying linearly along the beam length for different boundary constraints

BCs	α	Mode	[31]	[33]	[34]	Present	Δ ([31]), %
C–F	0.2	1	2.6863	2.6863	2.6873	2.68633	0.0011
		2	17.7501	17.7501	17.7225	17.75011	0.0001
		3	50.3934	–	50.2194	50.39258	0.0016
	0.4	1	3.0486	3.0486	3.0877	3.04857	0.0010
		2	16.8571	16.8571	17.4061	16.85706	0.0002
		3	45.4003	–	47.2734	45.39956	0.0016
	0.6	1	3.5985	3.5985	3.7700	3.59847	0.0008
		2	15.9616	15.9616	17.6687	15.96156	0.0003
		3	40.1304	–	45.9613	40.12961	0.0020
	0.8	1	4.5695	4.5695	5.0458	4.57064	0.0249
		2	15.2955	15.2955	18.6877	15.30362	0.0531
		3	34.5521	–	46.5828	34.58256	0.0882
P–P	0.2	1	8.1462	8.1462	8.1682	8.14619	0.0001
		2	32.5123	32.5123	32.4133	32.51207	0.0007
		3	73.0959	–	72.8179	73.09331	0.0035
	0.4	1	7.1254	7.1254	7.3647	7.12540	0.0000
		2	28.5003	28.5003	29.7076	28.50006	0.0008
		3	64.0350	–	66.9202	64.03231	0.0042
	0.6	1	5.8868	5.8868	6.6732	5.88675	0.0008
		2	24.2469	24.2469	27.9493	24.24648	0.0017
		3	54.3126	–	63.3243	54.30922	0.0062
	0.8	1	4.2283	4.2284	6.1283	4.23710	0.2081
		2	19.5300	19.5302	27.2590	19.51399	0.0820
		3	43.3451	–	62.2530	43.37406	0.0668
C–C	*0.2	1	18.1996	18.1996	18.2779	18.19954	0.0003
		2	50.4565	50.4560	50.4430	50.45559	0.0018
		3	99.1474	–	98.2992	99.14075	0.0067
	0.4	1	15.8350	15.8350	16.7396	15.83492	0.0005
		2	44.0370	44.0371	46.3346	44.03592	0.0025
		3	86.6414	–	90.9806	86.63419	0.0083
	0.6	1	13.3238	13.3238	16.1771	13.32340	0.0030
		2	37.1104	37.1105	44.4245	37.10787	0.0068
		3	73.0375	–	86.8967	73.02611	0.0156
	0.8	1	10.5339	10.5343	16.6925	10.53166	0.0213
		2	29.2402	29.2419	44.9420	29.22110	0.0653
		3	57.3787	–	87.0576	57.35837	0.0354

$$\begin{bmatrix} A_{11}(\omega) & A_{12}(\omega) & A_{13}(\omega) & A_{14}(\omega) \\ A_{21}(\omega) & A_{22}(\omega) & A_{23}(\omega) & A_{24}(\omega) \\ A_{31}(\omega) & A_{32}(\omega) & A_{33}(\omega) & A_{34}(\omega) \\ A_{41}(\omega) & A_{42}(\omega) & A_{43}(\omega) & A_{44}(\omega) \end{bmatrix} \begin{pmatrix} W(0) \\ W(1) \\ W(2) \\ W(3) \end{pmatrix} = 0, \tag{22}$$

where the functions $A_{ij}(\omega)$ are polynomials of ω.

Finally, the eigenvalues are calculated as roots of the characteristic equation:

$$\det|A_{ij}(\omega)| = 0. \tag{23}$$

A computational program has been developed within the Matlab environment to implement the DTM for solving the free vibration problem of inhomogeneous non-uniform FGP beams. The eigenvalue problem is solved using the standard algorithms provided by the Matlab package [59].

Results and Discussion

Verification

To verify the DTM adopted for solving the free vibration problem of inhomogeneous beams with non-uniform cross-sections, first, we examine various specific problems

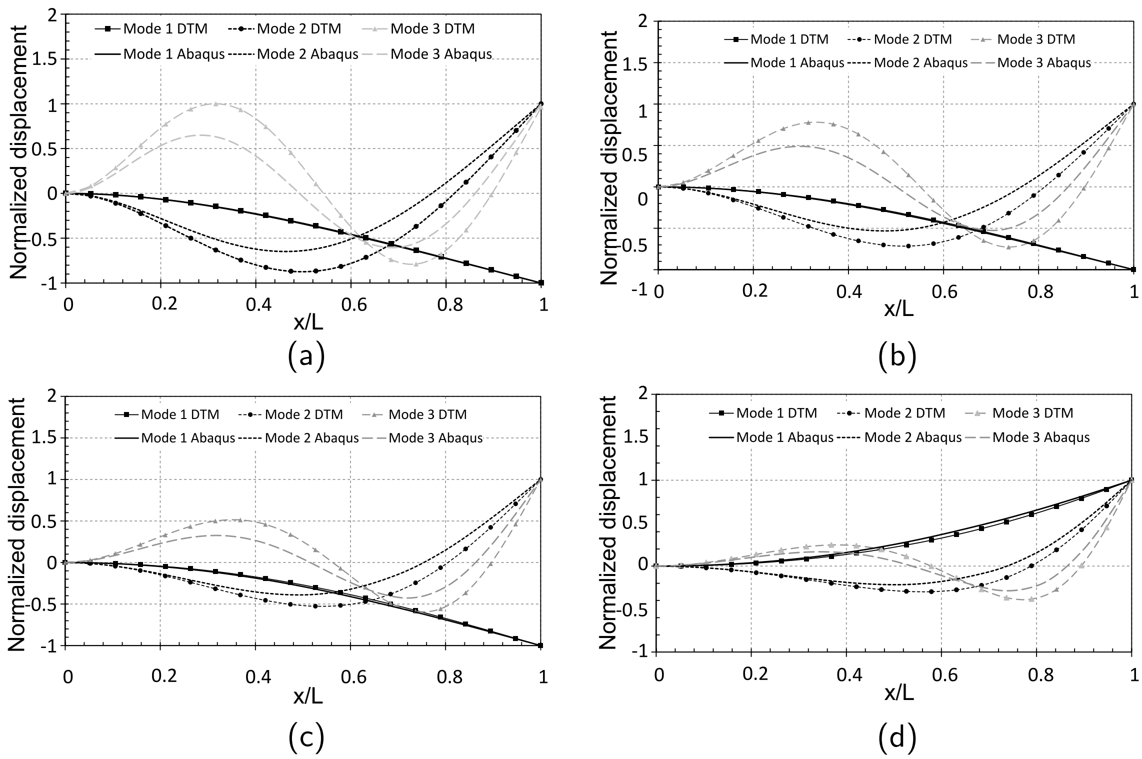

Fig. 4 The mode shapes associated with the first three natural frequencies for the cantilever double-tapered AFGM beam for different taper ratios: (a) α=0.2; (b) α=0.4; (c) α=0.6; and (d) α=0.8

and compare the results obtained with DTM with those available in the existing literature. In the calculations, we adhered to the recommendations comprehensively discussed in Ref. [32] for providing the fast convergence of the solutions and to ensure the reliability of the results. In addition, as the calculations involve finding roots of high-degree polynomials, which can potentially lead to computational instability, we have implemented strategies recommended in the MATLAB documentation to enhance stability in symbolic calculations. It included optimizing code, symbolically simplifying polynomial equations before finding their roots, and utilizing functions to fine-tune the root-finding process [59].

We start with free vibration analysis of double-tapered homogeneous beams with the height and width varying linearly along the x-coordinate. This implies that we have chosen $m = n = 1$ in (1). Assuming that the cross-sectional dimensions of the beam vary with the same taper parameters for both height and width $c_b = c_h = \alpha$, we can express (2) in the form: $\frac{A(x)}{A_0} = \left(1 - \alpha\frac{x}{L}\right)^2$ and $\frac{I(x)}{I_0} = \left(1 - \alpha\frac{x}{L}\right)^4$. The initial dimensions of the rectangular cross-section are taken as h_0 =0.01 m and b_0=0.03 m, and the length of the beam is L= 1 m. The material parameters for this beam are defined such that Young's modulus, E_0=210 GPa and the mass density, ρ_0=7800 kg/m^3.

The non-dimensional natural transverse frequencies are specified as $\bar{\omega}_n = \omega_n L^2\sqrt{\frac{\rho_0 A_0}{E_0 I_0}}$. Herein, A_0, I_0, E_0 and ρ_0 are beam's cross-section geometrical and material properties at $x = 0$, respectively. For the sake of verification, the first three non-dimensional natural frequencies computed with the proposed technique are compared with those found in Refs. [30] and [33] for a variety of boundary conditions such as cantilever beam (C-F), fully clamped beam (C–C) and pinned–pinned beam (P–P), and at different values of the taper ratio, α. The results are collected in Table 1.

One can see in Table 1 that the results obtained using different approaches exhibit a high degree of consistency. This indicates that the proposed computation method demonstrates considerable accuracy in predicting the natural frequencies of homogeneous beams with variable cross-sections.

Moreover, to validate the ability of the proposed method to accurately restore the sought function (21) from its respective sets of images (18), the mode shapes of beams associated with the first three natural frequencies of the cantilever double-tapered homogeneous beam are constructed. In addition, we utilized ABAQUS software [60] to conduct the frequency analysis for the same homogeneous beams with non-uniform cross-sections. The mode shapes of the beam have been modeled using the beam element "B22"

Table 3 Non-dimensional natural frequencies $\bar{\omega}_n$ of uniform FGP beams ($L/h = 10$) with even (type I), uneven symmetric (type II) and uneven non-symmetric (type IV) distributions for different porosity coefficients and boundary conditions

BCs	e_0	Mode	Type I			Type II			Type IV		
			[23]	Present	Δ,%	[23]	Present	Δ,%	[23]	Present	Δ,%
P–P	0.1	1	0.2751	0.26424	3.95	0.279	0.26813	3.90	0.2759	0.26506	3.93
		2	1.0463	1.05694	1.02	1.0593	1.07252	1.25	1.0487	1.06025	1.10
		3	2.1913	2.37812	8.53	2.2138	2.41316	9.01	2.1957	2.38556	8.65
	0.2	1	0.2701	0.25962	3.88	0.2785	0.26787	3.82	0.2721	0.26147	3.91
		2	1.0274	1.03849	1.08	1.0552	1.07150	1.54	1.0321	1.04587	1.33
		3	2.1518	2.33660	8.59	2.1995	2.41087	9.61	2.1606	2.35321	8.91
	0.3	1	0.2648	0.25475	3.80	0.2783	0.26793	3.73	0.2681	0.25786	3.82
		2	1.007	1.01898	1.19	1.0517	1.07173	1.90	1.0135	1.03145	1.77
		3	2.109	2.29271	8.71	2.1854	2.41140	10.34	2.122	2.32076	9.37
	0.4	1	0.2588	0.24956	3.57	0.2784	0.26843	3.58	0.264	0.25429	3.68
		2	0.9845	0.99826	1.40	1.049	1.07370	2.35	0.9923	1.01718	2.51
		3	2.062	2.24608	8.93	2.1718	2.41583	11.24	2.079	2.28865	10.08
	0.5	1	0.2523	0.24403	3.28	0.2791	0.26953	3.43	0.2598	0.25086	3.44
		2	0.9595	0.97613	1.73	1.0475	1.07814	2.93	0.9676	1.00342	3.70
		3	2.0096	2.19629	9.29	2.1586	2.42581	12.38	2.0301	2.25770	11.21
C–P	0.1	1	0.4169	0.41279	0.99	0.4222	0.41887	0.79	0.4179	0.41408	0.91
		2	1.2611	1.33769	6.07	1.2743	1.35740	6.52	1.2636	1.34188	6.19
		3	2.4225	2.79098	15.2	2.4422	2.83211	15.97	2.4263	2.79972	15.39
	0.2	1	0.4093	0.40558	0.91	0.4208	0.41847	0.55	0.4114	0.40846	0.71
		2	1.2384	1.31434	6.13	1.2664	1.35611	7.08	1.2434	1.32368	6.46
		3	2.3788	2.74226	15.3	2.4206	2.82942	16.89	2.3864	2.76176	15.73
	0.3	1	0.4012	0.39796	0.81	0.4196	0.41856	0.25	0.4044	0.40283	0.39
		2	1.2137	1.28965	6.26	1.2587	1.35641	7.76	1.2211	1.30543	6.91
		3	2.3315	2.69075	15.4	2.3983	2.83005	18.00	2.342	2.72367	16.27
	0.4	1	0.3922	0.38987	0.59	0.4188	0.41933	0.13	0.3964	0.39726	0.22
		2	1.1867	1.26342	6.46	1.2512	1.35890	8.61	1.1961	1.28737	7.63
		3	2.2795	2.63603	15.6	2.3751	2.83524	19.37	2.2938	2.68599	17.10
	0.5	1	0.3822	0.38122	0.26	0.4185	0.42106	0.61	0.3874	0.39188	1.16
		2	1.1565	1.23541	6.82	1.2441	1.36452	9.68	1.1674	1.26995	8.78
		3	2.2216	2.57759	16.0	2.3508	2.84696	21.11	2.2383	2.64966	18.38
C–C	0.1	1	0.5833	0.59899	2.69	0.5898	0.60782	3.06	0.5845	0.60087	2.80
		2	1.4759	1.65114	11.9	1.4883	1.67547	12.58	1.4783	1.65631	12.04
		3	2.6439	3.23690	22.4	2.6603	3.28460	23.47	2.6472	3.24703	22.66
	0.2	1	0.5728	0.58853	2.75	0.5867	0.60724	3.50	0.5752	0.59272	3.05
		2	1.4493	1.62232	11.9	1.4757	1.67388	13.43	1.4541	1.63385	12.36
		3	2.5963	3.18039	22.5	2.6309	3.28148	24.73	2.6031	3.20300	23.05
	0.3	1	0.5613	0.57748	2.88	0.5838	0.60738	4.04	0.5649	0.58455	3.48
		2	1.4204	1.59184	12.1	1.462	1.67425	14.47	1.4277	1.61132	12.86
		3	2.5446	3.12065	22.6	2.5999	3.28221	26.24	2.5552	3.15883	23.62
	0.4	1	0.5488	0.56574	3.09	0.5811	0.60849	4.71	0.5533	0.57646	4.19
		2	1.3887	1.55947	12.3	1.4491	1.67733	15.75	1.3983	1.58903	13.64
		3	2.4879	3.05719	22.9	2.5668	3.28823	28.11	2.5024	3.11513	24.49
	0.5	1	0.5349	0.55319	3.42	0.5787	0.61100	5.58	0.54000	0.56866	5.31
		2	1.3535	1.52490	12.7	1.43500	1.68426	17.37	1.36490	1.56753	14.85
		3	2.4247	2.98941	23.3	2.5311	3.30182	30.45	2.4433	3.07299	25.77

Table 4 Non-dimensional natural frequencies $\bar{\omega}_n$ of non-uniform FGP beams with tapered width for different porosity distributions, porosity coefficients, and boundary conditions

BCs	Mode	C–C				C–P				C–F				P–P			
e_0		Type I	Type II	Type III	Type IV	Type I	Type II	Type III	Type IV	Type I	Type II	Type III	Type IV	Type I	Type II	Type III	Type IV
0.0	1	22.35282	22.35282	22.35282	22.35282	15.64401	15.64401	15.64401	15.64401	3.76286	3.76286	3.76286	3.76286	9.86480	9.86480	9.86480	9.86480
	2	61.64497	61.64497	61.64497	61.64497	50.17667	50.17667	50.17667	50.17667	22.50181	22.50181	22.50181	22.50181	39.48290	39.48290	39.48290	39.48290
	3	120.87284	120.87284	120.87284	120.87284	104.46013	104.46013	104.46013	104.46013	62.15252	62.15252	62.15252	62.15252	88.83355	88.83355	88.83355	88.83355
0.2	1	21.58859	22.29106	20.99966	21.75797	15.10915	15.60079	14.69698	15.22769	3.63421	3.75246	3.53507	3.66272	9.52752	9.83754	9.26762	9.60227
	2	59.53737	61.47465	57.91321	60.00447	48.46117	50.03804	47.13916	48.84136	21.73249	22.43964	21.13963	21.90299	38.13301	39.37381	37.09275	38.43218
	3	116.74028	120.53887	113.55563	117.65615	100.88871	104.17151	98.13649	101.68022	60.02756	61.98079	58.39003	60.49850	85.79639	88.58811	83.45589	86.46950
0.4	1	20.68698	22.33692	19.42082	21.16105	14.47814	15.63288	13.59199	14.80993	3.48243	3.76018	3.26929	3.56224	9.12962	9.85778	8.57084	9.33884
	2	57.05088	61.60112	53.55904	58.35830	46.43725	50.14098	43.59503	47.50144	20.82486	22.48581	19.55026	21.30210	36.54044	39.45482	34.30395	37.37782
	3	111.86478	120.78686	105.01802	114.42836	96.67523	104.38583	90.75816	98.89071	57.52059	62.10831	54.00001	58.83878	82.21322	88.77036	77.18131	84.09728
0.6	1	19.56369	22.59827	17.50570	20.61302	13.69199	15.81579	12.25166	14.42638	3.29334	3.80418	2.94690	3.46998	8.63389	9.97312	7.72565	9.09698
	2	53.95305	62.32186	48.27749	56.84692	43.91574	50.72763	39.29605	46.27124	19.69409	22.74889	17.62238	20.75041	34.55631	39.91644	30.92118	36.40980
	3	105.79059	122.20008	94.66202	111.46486	91.42583	105.60715	81.80834	96.32961	54.39726	62.83498	48.67498	57.31496	77.74910	89.80898	69.57033	81.91931
0.8	1	17.99486	23.40562	15.03206	20.31329	12.59401	16.38083	10.52045	14.21661	3.02924	3.94009	2.53049	3.41953	7.94153	10.32942	6.63398	8.96471
	2	49.62651	64.54840	41.45565	56.02033	40.39410	52.53995	33.74333	45.59842	18.11480	23.56163	15.13225	20.44869	31.78521	41.34252	26.55187	35.88038
	3	97.30716	126.56585	81.28582	109.84409	84.09432	109.38012	70.24843	94.92892	50.03510	65.07985	41.79697	56.48156	71.51433	93.01754	59.73971	80.72815

provided by the package. The comparisons of both computations for each taper ratio of the beam are depicted in Fig. 3.

The plots of the mode shapes demonstrate a high degree of consistency for each of three frequencies across all taper ratio cases. Thus, the precision of the computed natural frequencies plays a primary role in the accuracy of mode shape restoration in the DTM.

Next, we calculate the natural frequencies of the same double tapered beam with linear variations in height and width, that is using $\frac{A(x)}{A_0} = \left(1 - \alpha\frac{x}{L}\right)^2$ and $\frac{I(x)}{I_0} = \left(1 - \alpha\frac{x}{L}\right)^4$. In addition to these geometric variations, we also account for the axial variation of the beam's material properties. Specifically, we consider the axially varying profiles of the Young's modulus $\frac{E(x)}{E_0} = \left(1 + \frac{x}{L}\right)$ and the mass density $\frac{\rho(x)}{\rho_0} = \left(1 + \frac{x}{L} + \left(\frac{x}{L}\right)^2\right)$. The comparisons of first three non-dimensional natural transverse frequencies $\bar{\omega}_n$ computed with the DTM and those found in Refs. [31, 33, 34] for different boundary conditions and a variety of taper ratios are presented in Table 2.

Table 2 clearly demonstrates that the results match well among the four different approaches. This fact provides strong evidence for the ability of the proposed technique to accurately predict the natural frequencies of inhomogeneous beams with cross-sections varying along the beam's length. In addition, it is worth noting that the Euler–Bernoulli model employed in the present calculations is suitable for our low-frequency analysis of slender beams.

In line with the previous example, we aimed to compare the mode shapes of the non-uniform AFGM beam, calculated using the DTM, with those obtained from ABAQUS to assess their accuracy. It's important to mention that ABAQUS, utilizing the user-defined subroutine UMAT, enables the vibration analysis of FGM structures with constant thickness, as discussed in Ref. [61]. The recent expansion of this modeling technique to non-uniform FGM beams is elaborated in Ref. [62]. Utilizing these advancements, we computed the mode shapes for the non-uniform AFGM beam under investigation and their comparisons with those derived using the DTM are illustrated in Fig. 4

The plots clearly illustrate that the mode shapes of the non-uniform AFGM beams, for both of the modeling approaches, exhibit good agreement across all the taper ratio cases and for each of the three natural frequencies.

The accuracy of the presented computation approach in calculating natural frequencies of FGP beams is assessed further. In this respect, an FGP beam of length L= 1 m and a square cross-section, which is composed of the open-cell metallic foam with $E_0 = 200$ GPa, $\rho_0 = 7850$ kg/m^3, and Poisson ratio equal to 1/3 is considered. The test problem provides a comparison of the first three non-dimensional

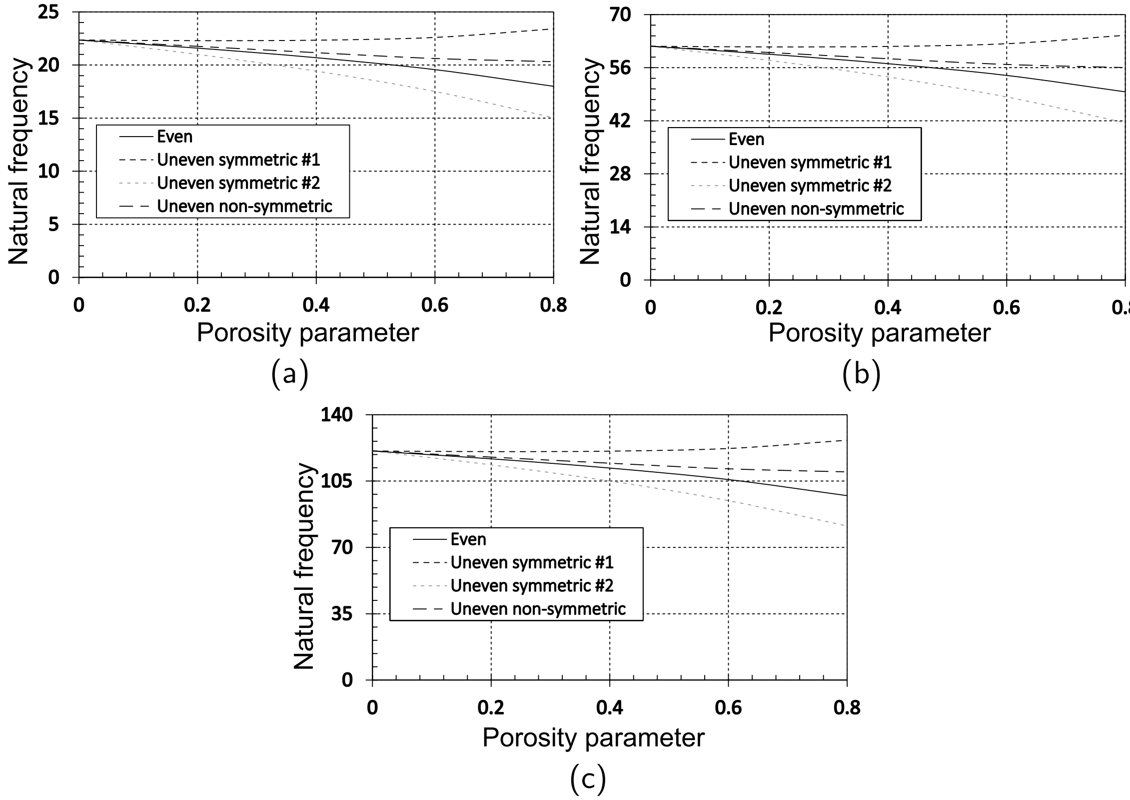

Fig. 5 Non-dimensional natural frequencies $\bar{\omega}_n$ versus porosity coefficients for the C–C supported FGP beams with tapered width: (a) 1–st frequency; (b) 2–nd frequency; and (c) 3–rd frequency

natural frequencies $\bar{\omega}_n = \omega_n L\sqrt{\frac{\rho_0(1-\nu^2)}{E_0}}$ of a uniform FGP beam at the beam aspect ratio L/h =10. The FGP beam is assumed to be subjected to three distinct porosity distributions such as even (type I), uneven symmetric (type II), and uneven non-symmetric (type IV) profiles. The calculations are performed for various porosity coefficient e_0 and different types of boundary conditions. The comparisons of the natural frequencies obtained in the present work and those available in Ref. [23] are presented in Table 3.

As observed in Table 3, the results exhibit good agreement for the first and, in some cases, the second natural frequencies across all boundary conditions and porosity coefficient values. However, notable discrepancies are observed for the third frequency. This discrepancy is attributed to the use of the third-order shear deformation theory for the FGP beam within the framework of the Chebyshev collocation method in Ref. [23]. This contrasts with the Euler–Bernoulli beam model used in our study, which neglects shear deformation and rotational effects in beam behavior. Nevertheless, the calculations in this study, which are based on the assumption of an initially planar cross-section remaining planar after deformation, offer practical engineering solutions for such structures with an emphasis on the simplicity and practicality of the Euler–Bernoulli beam model.

Parameter Study

Further, we use the proposed approach implementing the DTM to calculate natural frequencies of a series of non-uniform rectangular cross-section FGP beams. This includes cases with tapered width but constant height, tapered height but constant width, and double tapering with both height and width simultaneously. In the calculations, all four types of porosity profiles conditions through the beam thickness are taken into account. The material and geometrical properties of the FGP beams remain the same as those used in the previous test problems. The FGP beams under four types boundary and four values of non-zero porosity coefficients are investigated.

Let us consider a non-uniform FGP beam of length L= 1 m with a constant height h_0 and a width $b(x)$ that varies linearly with the x-coordinate. In other words, the cross-section characteristics are expressed as $\frac{A(x)}{A_0} = \frac{I(x)}{I_0} = \left(1 - \alpha\frac{x}{L}\right)$. It is assumed that the beam aspect ratio is L/h= 20 and the taper ratio is α= 0.2. Table 4

Table 5 Non-dimensional natural frequencies $\bar{\omega}_n$ of non-uniform FGP beams with tapered height for different porosity distributions, porosity coefficients, and boundary conditions

BCs	Mode	C–C				C–P				C–F				P–P			
e_0		Type I	Type II	Type III	Type IV	Type I	Type II	Type III	Type IV	Type I	Type II	Type III	Type IV	Type I	Type II	Type III	Type IV
0.0	1	20.07821	20.07821	20.07821	20.07821	14.25757	14.25757	14.25757	14.25757	3.60827	3.60827	3.60827	3.60827	8.84619	8.84619	8.84619	8.84619
	2	55.33995	55.33995	55.33995	55.33995	45.24435	45.24435	45.24435	45.24435	20.62102	20.62102	20.62102	20.62102	35.44524	35.44524	35.44524	35.44524
	3	108.48302	108.48302	108.48302	108.48302	93.95363	93.95363	93.95363	93.95363	56.19228	56.19228	56.19228	56.19228	79.73034	79.73034	79.73034	79.73034
0.2	1	19.39175	19.86667	18.92037	19.50859	13.77012	14.13214	13.42065	13.85825	3.48491	3.60085	3.38360	3.51239	8.54375	8.74674	8.33648	8.59367
	2	53.44791	54.74627	52.14881	53.76730	43.69747	44.78277	42.62065	43.96351	19.91600	20.45251	19.40142	20.04604	34.23339	35.06009	33.39945	34.43655
	3	104.77406	107.31033	102.22756	105.39795	90.74142	92.96162	88.52098	91.28660	54.27110	55.63527	52.92178	54.60474	77.00441	78.86314	75.13036	77.46138
0.4	1	18.58188	19.72840	17.58706	18.92858	13.19503	14.06513	12.45521	13.45286	3.33937	3.61427	3.12297	3.41627	8.18693	8.67875	7.74972	8.33622
	2	51.21573	54.35300	48.47451	52.16541	41.87251	44.49143	39.59815	42.66003	19.08423	20.37225	17.99373	19.46298	32.80368	34.80353	31.04411	33.40884
	3	100.39831	106.52919	95.02537	102.25502	86.95172	92.31520	82.26462	88.57073	52.00454	55.29450	49.15310	52.98993	73.78842	78.28412	69.83444	75.14959
0.6	1	17.57290	19.75823	16.00295	18.38003	12.47855	14.12841	11.30487	13.07203	3.15804	3.67093	2.80952	3.32855	7.74238	8.68360	7.05312	8.09206
	2	48.43475	54.42083	44.11009	50.64923	39.59886	44.58808	36.00492	41.42875	18.04797	20.48697	16.31485	18.91657	31.02246	34.84312	28.24700	32.43561
	3	94.94675	106.65009	86.47129	99.27929	82.23030	92.46119	74.83094	86.00176	49.18073	55.44404	44.67074	51.46623	69.78176	78.36926	63.54516	72.96021
0.8	1	16.16371	20.27154	14.03536	18.03643	11.47788	14.55883	9.86752	12.84131	2.90480	3.84314	2.41008	3.28330	7.12152	8.89893	6.18991	7.93713
	2	44.55073	55.81762	38.69226	49.69602	36.42339	45.79555	31.53674	40.66218	16.60069	21.14765	14.21309	18.58970	28.53474	35.73638	24.77735	31.82224
	3	87.33289	109.37309	75.85522	97.40554	75.63619	94.88562	65.59790	84.39161	45.23689	56.99237	39.09181	50.52275	64.18590	80.37043	55.74277	71.57998

presents the first three dimensionless natural frequencies, normalized as $\bar{\omega}_n = \omega_n \frac{L^2}{h_0}\sqrt{\frac{12\rho_0}{E_0}}$.

To better illustrate the influence of porosity on the free vibration of the non-uniform beams, we have generated graphs using the data provided in Table 4. These graphs depict non-dimensional natural frequencies plotted versus the porosity coefficient. Our analysis revealed that the first three frequencies of the porous beams exhibit similar trends for all considered boundary conditions. As a result, to limit the volume of the present paper, only findings pertaining to C–C constraints are presented in Fig. 5.

It is evident from the plots that the three natural frequencies, depending on the type of porosity distribution, demonstrate similar patterns of changes as the porosity coefficient increases. These changes exhibit similar trends across all kind of supports. Specifically, for the FGP beam with uneven symmetric (type II) distributions, the natural frequencies slightly increase as the porosity increases. On the other hand, for the FGP beams with the other types of distributions, the natural frequencies decrease as the porosity increases. This behavior can be attributed to the fact that, as the porosity coefficient rises, both beam stiffness and cross-sectional inertia decrease. However, in the case of uneven symmetric (type II) distribution, the reduction rate in beam stiffness is smaller than that in inertia, while in the other distributions, the opposite relationship holds. Remarkably, among the various profiles considered, the FGP beam with an uneven non-symmetric (type IV) profile shows the least decrease in natural frequencies. In contrast, the beam with an uneven symmetric (type III) profile experiences the most significant reduction compared to the other profiles.

The other study deals with non-uniform FGP beams of constant width b_0 and height $h(x)$ linearly varying with x-coordinate such that Eq. 2 take a form: $\frac{A(x)}{A_0} = \left(1 - \alpha\frac{x}{L}\right)$, $\frac{I(x)}{I_0} = \left(1 - \alpha\frac{x}{L}\right)^3$ with α=0.2. Table 5 collects the first three dimensionless natural frequencies for mentioned above four porosity profiles, considering four types of imposed boundary conditions and accounting for a range of porosity coefficients.

Similarly to the previous example, Fig. 6 presents plots of natural frequencies against porosity coefficient values, extracted from Table 5 for the beam clamped at both ends. Once more, these plots are necessary to clarify the influence of porosity on the free vibration characteristics of height-tapered porous beams.

Upon analyzing the plots presented in Fig. 5, it becomes apparent that while the natural frequencies differ from those observed in the case of the beam with tapered width, they exhibit similar trends in terms of frequency changing patterns as the porosity coefficient increases. Particularly, in the case of FGP beams with uneven symmetric (type II)

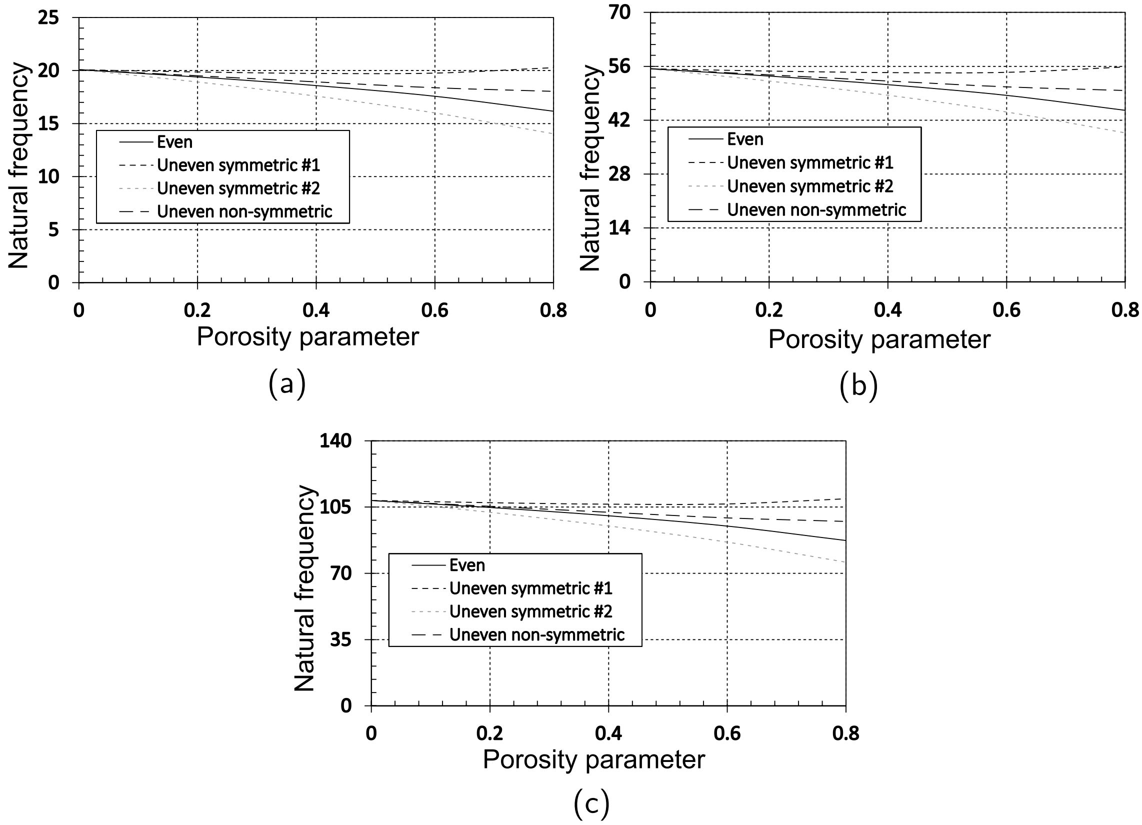

Fig. 6 Non-dimensional natural frequencies $\bar{\omega}_n$ versus porosity coefficients for the C–C supported FGP beams with tapered height: (a) 1–st frequency; (b) 2–nd frequency; and (c) 3–rd frequency

distributions, the natural frequencies slightly increase with growing the porosity coefficient. Conversely, for FGP beams with other types of distributions, the natural frequencies decrease with an increase in porosity. Once again, the FGP beams with uneven non-symmetric (type IV) profiles experience a comparatively smaller decrease in natural frequencies compared to the other porosity distributions. Changing the boundary conditions among those considered does not alter the observed frequency trends as the porosity coefficient increases for the specified porosity distributions.

Last, non-uniform FGP beams with simultaneous linear variation of width and height along the x-coordinate are investigated. The cross-section parameters of the beams are defined as $\frac{A(x)}{A_0} = \left(1 - \alpha \frac{x}{L}\right)^2, \frac{I(x)}{I_0} = \left(1 - \alpha \frac{x}{L}\right)^4$, where α=0.2. The first three non-dimensional natural frequencies for the specified range of the porosity profiles, boundary conditions, and porosity coefficient values are arranged in Table 6.

Figure7 shows plots of the natural frequencies versus the porosity coefficient for C–C boundary conditions, corresponding to the data in Table6. These plots clearly depict how porosity affects the natural frequencies of double-tapered beams. It is worth noting that similar trends are observed for the beams subjected to boundary conditions other than the shown clamped–clamped case for all three frequencies.

These plots do not exhibit any new aspects in frequency variations with the increase of the porosity parameter when compared to the observations in the previous two types of porous beams, namely those tapered with width and those tapered with height individually. This fact shows that the type of porosity profile is a dominant factor affecting the dynamic response of the tapered beams.

In addition, the data in Tables 4–6 are rearranged into plots to facilitate the comparison of the natural frequency versus porosity coefficient relationships between the beams of different taper shapes, porosity profiles, and boundary conditions. Each plot depicts frequency-porosity curves for FGP beams with distinct non-uniform geometries, including uniform, width-tapered, height-tapered, and double-tapered shapes. The plots are organized in alignment with four different porosity profiles, spanning from type I to type IV, all associated with a specific natural frequency.

In Fig. 8, one can see plots of non-dimensional natural frequencies ($\bar{\omega}_n$) as they vary with porosity coefficients for clamped–clamped FGP beams of different taper shapes and porosity profiles. Each row corresponds to a specific frequency.

Table 6 Non-dimensional natural frequencies $\bar{\omega}_n$ of double-tapered FGP beams for different porosity distributions, porosity coefficients, and boundary conditions

BCs	Mode	C–C				C–P				C–F				P–P			
e_0		Type I	Type II	Type III	Type IV	Type I	Type II	Type III	Type IV	Type I	Type II	Type III	Type IV	Type I	Type II	Type III	Type IV
0.0	1	20.09663	20.09663	20.09663	20.09663	14.47057	14.47057	14.47057	14.47057	3.85512	3.85512	3.85512	3.85512	8.82458	8.82458	8.82458	8.82458
	2	55.36495	55.36495	55.36495	55.36495	45.46662	45.46662	45.46662	45.46662	21.05675	21.05675	21.05675	21.05675	35.46564	35.46564	35.46564	35.46564
	3	108.51043	108.51043	108.51043	108.51043	94.18341	94.18341	94.18341	94.18341	180.61078	180.61078	180.61078	180.61078	79.76244	79.76244	79.76244	79.76244
0.2	1	19.40954	19.88739	18.93652	19.52703	13.97583	14.34379	13.62102	14.06540	3.72331	3.84673	3.61529	3.75257	8.52287	8.72423	8.31672	8.57243
	2	53.47206	54.77439	52.17073	53.79233	43.91215	45.00491	42.82903	44.17996	20.33683	20.88463	19.81143	20.46962	34.25309	35.08136	33.41809	34.45661
	3	104.80053	107.34113	102.25158	105.42538	90.96334	93.19162	88.73620	91.51043	54.69419	56.07055	53.33356	55.03077	77.03541	78.89659	75.15970	77.49293
0.4	1	18.59892	19.75205	17.60038	18.94716	13.39215	14.27640	12.64096	13.65412	3.56781	3.86050	3.33711	3.64976	8.16692	8.65499	7.73217	8.31530
	2	51.23887	54.38505	48.49258	52.19063	42.07822	44.71473	39.79035	42.87065	19.48749	20.80262	18.37407	19.87423	32.82256	34.82602	31.06065	33.42860
	3	100.42368	106.56430	95.04518	102.28266	87.16438	92.54684	82.46285	88.78863	52.40996	55.72903	49.53448	53.40378	73.81813	78.31945	69.86048	75.18065
0.6	1	17.58901	19.78578	16.01250	18.39901	12.66497	14.34134	11.47311	13.26779	3.37408	3.92028	3.00260	3.55588	7.72347	8.65795	7.03836	8.07134
	2	48.45664	54.45814	44.12302	50.67496	39.79340	44.81515	36.17755	41.63409	18.42933	20.91967	16.65981	19.31626	31.04032	34.86744	28.26089	32.45520
	3	94.97074	106.69096	86.48547	99.30749	82.43141	92.69731	75.00859	86.21433	49.56414	55.88224	45.01577	51.86876	69.80986	78.40743	63.56706	72.99100
0.8	1	16.17854	20.30500	14.03919	18.05639	11.64935	14.77901	10.01365	13.03390	3.10351	4.10307	2.57644	3.50728	7.10412	8.86987	6.17899	7.91618
	2	44.57086	55.86288	38.69740	49.72307	36.60233	46.03320	31.68416	40.86487	16.95147	21.59415	14.51378	18.98246	28.55117	35.76400	24.78756	31.84206
	3	87.35495	109.42266	75.86086	97.43518	75.82117	95.13356	65.74892	84.60163	45.58955	57.44646	39.39104	50.91876	64.21175	80.41372	55.75893	71.61113

Analyzing the plots in Fig. 8, we revealed that, first, the geometric shapes of the FGP beams affect the natural frequencies. The frequencies of uniform and width-tapered beams have values close to each other, while, in turn, the frequencies of height-tapered and double-tapered beams are closely aligned but lower than those in the two previous beams. That is, the height taper ratio has a more pronounced effect on the natural frequencies compared to the width taper ratio. This is attributed to the fact that varying a height along the beam length directly impact the bending stiffness, leading to notable alterations in the natural frequencies. On the other hand, variations in the width taper ratio primarily affect the cross-sectional area that has a comparatively smaller impact on the natural frequencies [30].

Second, the porosity profile plays a significant role in the dynamic response of the beams of all shapes. In particular, for the FGP beams with an uneven symmetric profile with stiffer layers in the surface area (type II), all the first three natural frequencies exhibit a slight increase with an increase in the porosity coefficient. On the other hand, for beams with other porosity profiles, the frequencies decrease as the coefficient increases.

Arranging the non-dimensional natural frequencies ($\bar{\omega}_n$) versus porosity coefficients for FGP beams with P–P and C–P supports in a manner similar to the plots in Fig. 8, we found out that these boundary conditions did not alter the trends observed in the frequency-porosity curves of the fully clamped FGP beam. As these plots do not provide new insights, we have not included them in the current context.

In the case of the cantilever FGP beam, the variations of the frequency-porosity curves resemble those in the FGP beams with C–C, P–P and C–P supports. However, the influence of the geometric shape on the natural frequencies is more pronounced for this beam type with all kinds of the porosity profiles as shown in Fig. 9. Specifically, the fundamental frequency, and to a lesser extent, the second frequency, exhibit notably distinct values depending on the beam shape.

Conclusions

The primary objective of this study is to examine the free vibration characteristics of beams with non-uniform cross-sections varying along the beam length, while the beams are composed of materials with functionally graded porosity changing across the beam thickness. The main focus is on calculating the natural frequencies of these beams under different boundary conditions and different types of the porosity profiles. In this study, the classical Euler–Bernoulli beam theory and Hamilton's principle are utilized to derive the governing equation of motion for the beams. Subsequently, the differential transformation method is employed

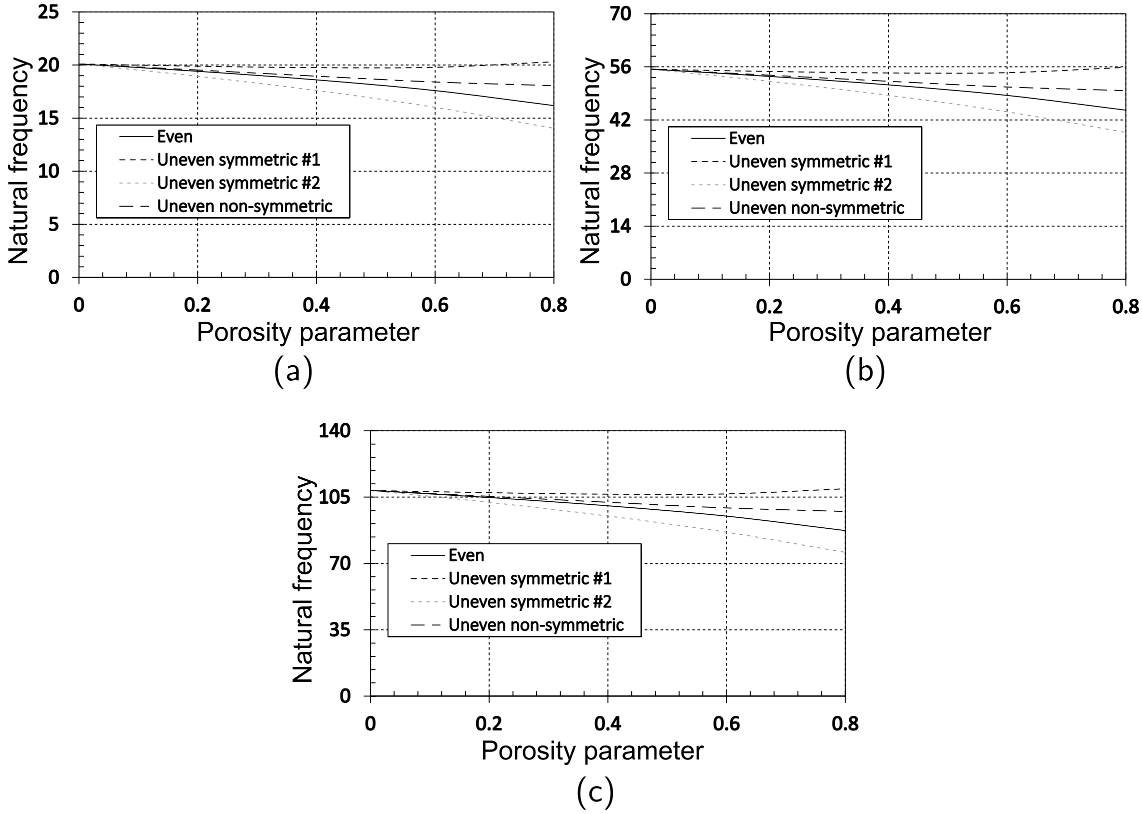

Fig. 7 Non-dimensional natural frequencies $\bar{\omega}_n$ versus porosity coefficients for the double-tapered C–C supported FGP beams: (a) 1–st frequency; (b) 2–nd frequency; and (c) 3–rd frequency

to solve this equation. This method, known as a semi-analytic approach to solving differential equations with variable coefficients, not only enhances computational accuracy but also reduces the computational cost compared to numerical methods such as the finite-element method. To validate the proposed technique, verification examples are provided, demonstrating the accuracy of the results of calculations. In summary, the results obtained from the parametric studies conducted in this research can be summarized as follows:

- the presence of porosity and variations in geometry affect the free vibration of the beams under different support conditions, leading to alternations in their behavior compared to that of homogeneous uniform beams;
- taper parameters have been observed to influence the vibration behaviors of the porous FGM beam in distinct ways. Specifically, the height taper ratio has a dominant effect on the transverse vibration, while the width taper ratio has a lesser impact on it;
- various porosity profiles exhibit distinct effects on the natural frequencies of the FGP beams, resulting in diverse alterations in the relationships between frequencies and porosity coefficient;
- the uneven symmetric porosity distribution with stiffer layer in central area of the cross-section (type III) affects the natural frequencies of the beam more significantly than the other porosity profiles for all types of boundary constraints;
- the porosity profile in the form of uneven symmetric with stiffer layers in surface areas (type II) lead to improved performance of the beams, resulting in less variation in the natural frequencies with increasing porosity coefficient for all types of boundary constraints;
- while the natural frequencies of FGP beams with uneven non-symmetric porosity profiles (type IV) are more sensitive to changes with growing the porosity compared to the beams with porosity profile type II, this porosity distribution causes a smaller decrease in the frequencies with increasing coefficient values compared to the porosity defined by an even pattern (type I) for all types of boundary constraints;
- while the present beam model, developed using the simplest Euler–Bernoulli assumptions, provides reasonably accurate results, it may not be entirely suitable for sufficiently thick beams and definitely not for high frequency vibrations, i.e., the height to wavelength has to be small too. For enhanced accuracy, it is advisable to consider employing the Timoshenko beam theory or high-order shear deformation theories.

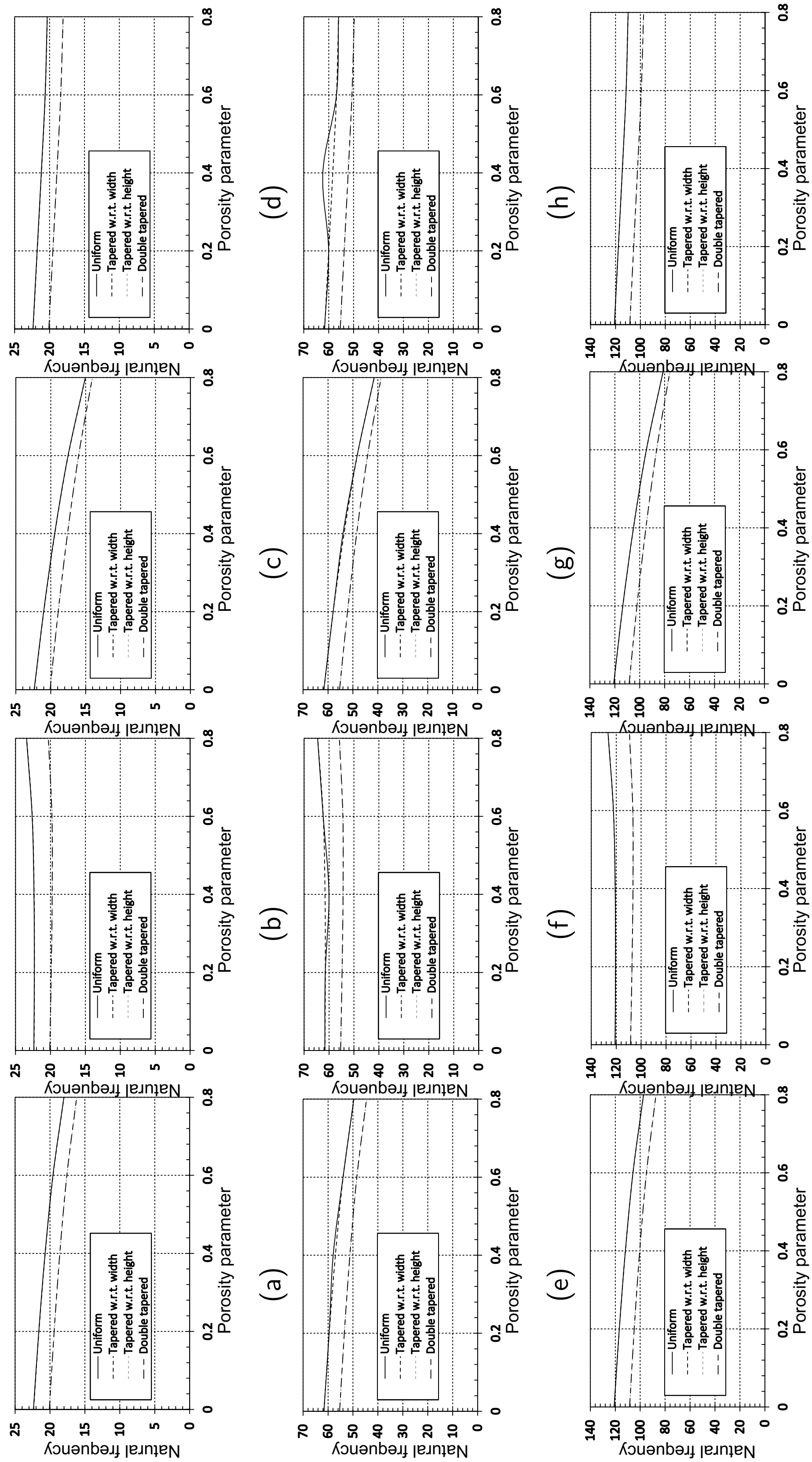

Fig. 8 Non-dimensional natural frequencies $\bar{\omega}_n$ versus porosity coefficients for C–C supported FGP beams of various taper shapes and porosity profiles: (a)–(d) 1–st frequency; (e)–(h) 2–nd frequency; and (i)–(l) 3–rd frequency

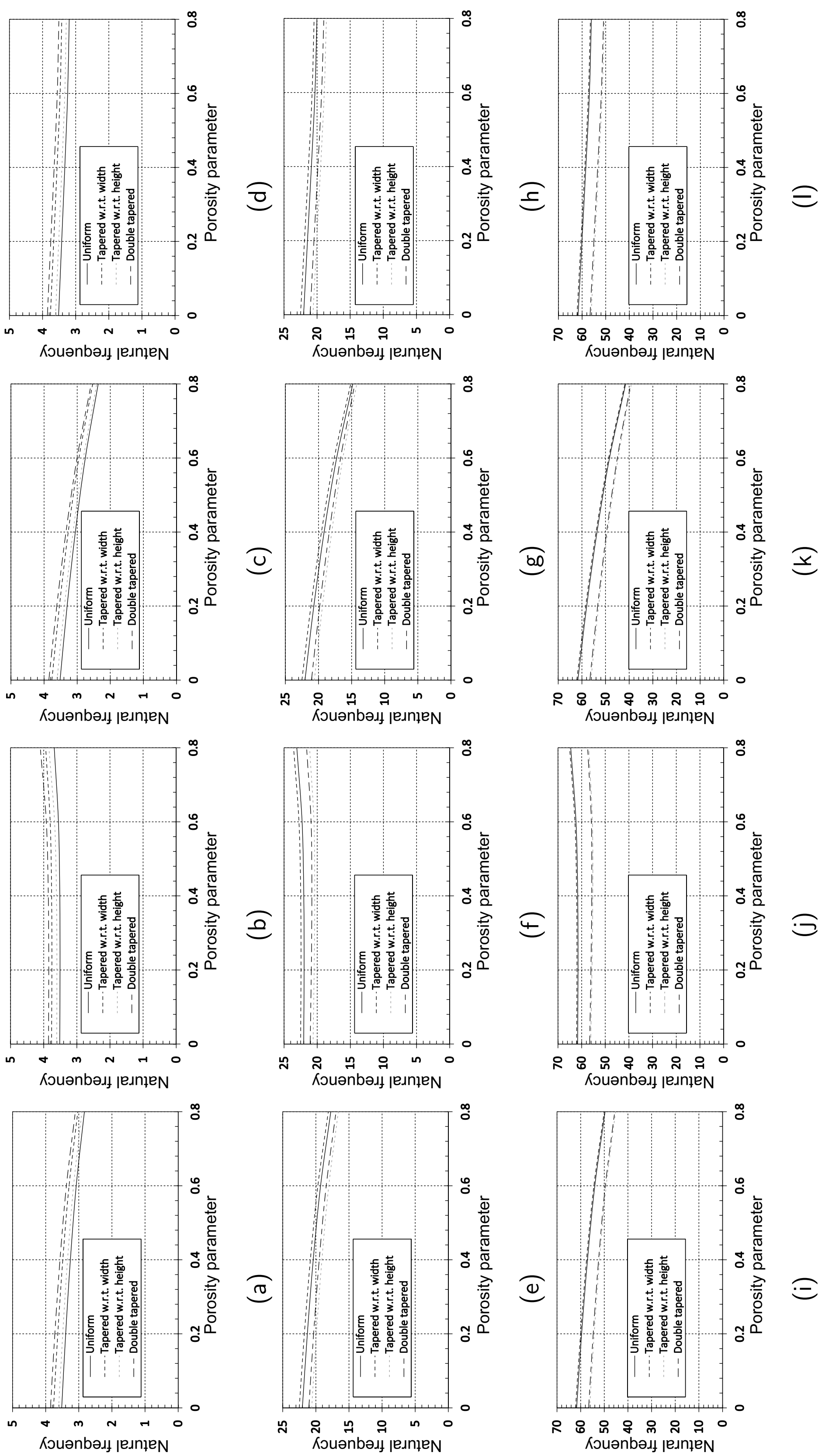

Fig. 9 Non-dimensional natural frequencies $\bar{\omega}_n$ versus porosity coefficients for C–F supported FGP beam of various taper shapes and porosity profiles: (a)–(d) 1–st frequency; (e)–(h) 2–nd frequency; and (i)–(l) 3–rd frequency

These results unequivocally highlight the importance of carefully selecting geometrical parameters and porosity profiles during the performance design process of FG porous beams. In this regard, the DTM proves to be an effective and accurate method for computing the natural frequencies of such beams.

Appendix A

The averaged Young's modulus $E_z(x)$ and mass density $\rho_z(x)$ in (16) determined by analytically integrating Eq. (11) over the rectangular domain $A(x)$ for every porosity profile type (3)–(6) are presented as follows:

$$E_z(x) = E_0\left(1 - e_0\alpha(x)\right),$$
$$\rho_z(x) = \rho_0\left(1 - e_m\alpha_*(x)\right)$$

– Type I:

$$\alpha(x) = \frac{1}{e_0} - \frac{1}{e_0}\left(\frac{2}{\pi}\sqrt{1-e_0} - \frac{2}{\pi} + 1\right)^2, \quad \alpha_*(x) = \frac{2}{\pi} \tag{A.1}$$

– Type II:

$$\alpha(x) = \frac{3}{\delta(x)}\left[\left(1 - \frac{2}{\delta^2(x)}\right)\sin\delta(x) + \frac{2}{\delta(x)}\cos\delta(x)\right], \quad \alpha_*(x) = \frac{\sin\delta(x)}{\delta(x)}, \tag{A.2}$$

where $\delta(x) = \frac{\pi h(x)}{2h_0}$

– Type III:

$$\alpha(x) = \frac{3}{\delta(x)}\left[-\cos\delta(x) + \frac{2}{\delta(x)}\sin\delta(x) - \frac{2}{\delta^2(x)}(1-\cos\delta(x))\right], \quad \alpha_*(x) = \frac{1-\cos\delta(x)}{\delta(x)} \tag{A.3}$$

– Type IV:

$$\alpha(x) = \frac{3}{\delta_1(x)}\left[\left(1 - \frac{2}{\delta_1^2(x)}\right)\sin\delta_1(x) + \frac{2}{\delta_1(x)}\cos\delta_1(x)\right]\cos\alpha_1, \quad \alpha_*(x) = \frac{\sin\delta_1(x)}{\delta_1(x)}\cos\alpha_1, \tag{A.4}$$

where $\delta_1(x) = \frac{\delta(x)}{2}\cos\alpha_1$

References

1. Wu H, Yang J, Kitipornchai S (2020) Mechanical analysis of functionally graded porous structures: A review. International Journal of Structural Stability and Dynamics 20(13):2041015
2. Burlayenko VN, Sadowski T (2011) Dynamic analysis of debonded sandwich plates with flexible core - Numerical aspects and simulation. In: Altenbach H, Eremeyev VA (eds) Shell-like Structures: Non-classical Theories and Applications, vol 15. Advanced Structured Materials. Springer, Berlin, Heidelberg, pp 415–440
3. Burlayenko VN, Altenbach H, Sadowski T (2019) Dynamic fracture analysis of sandwich composites with face sheet/core debond by the finite element method. In: Altenbach H, Belyaev A, Eremeyev VA, Krivtsov A, Porubov AV (eds) Dynamical Processes in Generalized Continua and Structures, vol 103. Advanced Structured Materials. Springer, Cham, pp 163–194
4. Vattré A, Pan E, Chiaruttini V (2021) Free vibration of fully coupled thermoelastic multilayered composites with imperfect interfaces. Composite Structures 259:113203
5. Wei L, Chen J (2022) Characterization of delamination features of orthotropic CFRP laminates using higher harmonic generation technique: Experimental and numerical studies. Composite Structures 285:115239
6. Huang B, Zhao G, Ren S, Chen W, Han W (2023) Higher-order model with interlaminar stress continuity for multi-directional FG-GRC porous multilayer panels resting on elastic foundation. Engineering Structures 286:116074
7. Sobczak JJ, Drenchev L (2013) Metallic functionally graded materials: A specific class of advanced composites. Journal of Materials Science and Technology 29(4):297–316
8. Xie K, Wang Y, Fan X, Fu T (2020) Nonlinear free vibration analysis of functionally graded beams by using different shear deformation theories. Applied Mathematical Modelling 77:1860–1880
9. Thai H-T, Kim S-E (2015) A review of theories for the modeling and analysis of functionally graded plates and shells. Composite Structures 128:70–86
10. Tornabene F, Fantuzzi N, Bacciocchi M (2014) Free vibrations of free-form doubly-curved shells made of functionally graded materials using higher-order equivalent single layer theories. Composites Part B: Engineering 67:490–509
11. Burlayenko VN, Sadowski T, Altenbach H (2022) Efficient free vibration analysis of FGM sandwich flat panels with conventional shell elements. Mechanics of Advanced Materials and Structures 29(25):3709–3726
12. Burlayenko VN (2021) A continuum shell element in layerwise models for free vibration analysis of FGM sandwich panels. Continuum Mechanics and Thermodynamics 33(4):1385–1407
13. Hirane H, Belarbi M-O, Houari MSA, Tounsi A (2022) On the layerwise finite element formulation for static and free vibration analysis of functionally graded sandwich plates. Engineering with Computers 38(5):3871–3899
14. Burlayenko VN, Sadowski T, Dimitrova S (2019) Three-dimensional free vibration analysis of thermally loaded FGM sandwich plates, Materials 12 (15)
15. Roshanbakhsh M, Tavakkoli S, Neya B Navayi (2020) Free vibration of functionally graded thick circular plates: An exact and three-dimensional solution, International Journal of Mechanical Sciences 188, 105967
16. Najibi A, Kianifar M, Ghazifard P (2023) Three-dimensional natural frequency investigation of bidirectional fg truncated thick hollow cone. Engineering Computations 40(1):100–125
17. Huang C-S, Huang SH (2020) Analytical solutions based on fourier cosine series for the free vibrations of functionally graded material rectangular mindlin plates, Materials 13 (17)

18. Wang Q, Li Q, Wu D, Yu Y, Tin-Loi F, Ma J, Gao W (2020) Machine learning aided static structural reliability analysis for functionally graded frame structures. Applied Mathematical Modelling 78:792–815
19. Njim E, Bakhy S, Al-Waily M (2021) Analytical and numerical free vibration analysis of porous functionally graded materials (FGPMs) sandwich plate using Rayleigh-Ritz method. Archives of Materials Science and Engineering 110(1):27–41
20. Burlayenko VN, Sadowski T, Altenbach H, Dimitrova S (2019) Three-dimensional finite element modelling of free vibrations of functionally graded sandwich panels. In: Altenbach H, Chróścielewski J, Eremeyev VA, Wiśniewski K (eds) Recent Developments in the Theory of Shells, vol 110. Advanced Structured Materials. Springer, Cham, pp 157–177
21. Liu J, Hao C, Ye W, Yang F, Lin G (2021) Free vibration and transient dynamic response of functionally graded sandwich plates with power-law nonhomogeneity by the scaled boundary finite element method. Computer Methods in Applied Mechanics and Engineering 376:113665
22. Chen D, Yang J, Kitipornchai S (2016) Free and forced vibrations of shear deformable functionally graded porous beams. International Journal of Mechanical Sciences 108–109:14–22
23. Wattanasakulpong N, Chaikittiratana A, Pornpeerakeat S (2018) Chebyshev collocation approach for vibration analysis of functionally graded porous beams based on third-order shear deformation theory. Acta Mechanica Sinica 34(6):1124–1135
24. Gao K, Li R, Yang J (2019) Dynamic characteristics of functionally graded porous beams with interval material properties. Engineering Structures 197:109441
25. Askari M, Brusa E, Delprete C (2021) On the vibration analysis of coupled transverse and shear piezoelectric functionally graded porous beams with higher-order theories. The Journal of Strain Analysis for Engineering Design 56(1):29–49
26. Nguyen N-D, Nguyen T-N, Nguyen T-K, Vo TP (2022) A new two-variable shear deformation theory for bending, free vibration and buckling analysis of functionally graded porous beams. Composite Structures 282:115095
27. Merdaci S, Adda HM, Hakima B, Dimitri R, Tornabene F (2021) Higher-order free vibration analysis of porous functionally graded plates, Journal of Composites Science 5 (11)
28. Abuteir BW, Boutagouga D (2022) Free-vibration response of functionally graded porous shell structures in thermal environments with temperature-dependent material properties. Acta Mechanica 233(11):4877–4901
29. Belarbi M-O, Daikh AA, Garg A, Hirane H, Houari MSA, Civalek O, Chalak HD (2022) Free-vibration response of functionally graded porous shell structures in thermal environments with temperature-dependent material properties. Archives of Civil and Mechanical Engineerin 23(1):15
30. Banerjee J, Su H, Jackson D (2006) Free vibration of rotating tapered beams using the dynamic stiffness method. Journal of Sound and Vibration 298(4):1034–1054
31. Rajasekaran S (2013) Differential transformation and differential quadrature methods for centrifugally stiffened axially functionally graded tapered beams. International Journal of Mechanical Sciences 74:15–31
32. Ghazaryan D, Burlayenko VN, Avetisyan A, Bhaskar A (2018) Free vibration analysis of functionally graded beams with non-uniform cross-section using the differential transform method. Journal of Engineering Mathematics 110(1):97–121
33. Liu P, Lin K, Liu H, Qin R (2016) Free transverse vibration analysis of axially functionally graded tapered Euler-Bernoulli beams through spline finite point method. Shock and Vibration 216:5891030
34. Cao D, Gao Y (2019) Free vibration of non-uniform axially functionally graded beams using the asymptotic development method. Applied Mathematics and Mechanics 40(1):85–96
35. Soltani M, Asgarian B (2019) New hybrid approach for free vibration and stability analyses of axially functionally graded Euler-Bernoulli beams with variable cross-section resting on uniform Winkler-Pasternak foundation. Latin American Journal of Solids and Structures 3(16):1–25
36. Li Z, Xu Y, Huang D (2021) Analytical solution for vibration of functionally graded beams with variable cross-sections resting on Pasternak elastic foundations. International Journal of Mechanical Sciences 191:106084
37. Chen Y, Dong S, Zang Z, Gao M, Zhang J, Ao C, Liu H, Zhang Q (2021) Free transverse vibrational analysis of axially functionally graded tapered beams via the variational iteration approach. Journal of Vibration and Control 27(11–12):1265–1280
38. Adelkhani R, Ghanbari J (2022) Vibration analysis of nonlinear tapered functionally graded beams using point collocation method. International Journal for Computational Methods in Engineering Science and Mechanics 23(4):334–348
39. Shen H, Ding L, Fan J, Wang M (2023) Research on dynamics of a rotating internal tapered fgm microbeam, Journal of the Brazilian Society of Mechanical Sciences and Engineering 45 (316)
40. Ebrahimi F, Hashemi M (2016) On vibration behavior of rotating functionally graded double-tapered beam with the effect of porosities. Proceedings of the Institution of Mechanical Engineers, Part G: Journal of Aerospace Engineering 230(10):1903–1916
41. Ebrahimi F, Hashemi M (2017) Vibration analysis of non-uniform imperfect functionally graded beams with porosities in thermal environment. Journal of Mechanics 33(6):739–757
42. Kien ND, Thom TT, Gan BS, Tuyen BV (2017) Influences of dynamic moving forces on the functionally graded porous-nonuniform beams. International Journal of Engineering and Technology Innovation 6(3):173–189
43. Tian J, Zhang Z, Hua H (2019) Free vibration analysis of rotating functionally graded double-tapered beam including porosities. International Journal of Mechanical Sciences 150:526–538
44. Sinha A (2021) Free vibration of an euler-bernoulli beam with arbitrary nonuniformities and discontinuities. AIAA Journal 59(11):4805–4808
45. Sinha A (2023) Free vibration of a timoshenko beam with arbitrary nonuniformities, discontinuities and constraints. Journal of Vibration Engineering and Technologies 11(5):2099–2108
46. Huang H, Gao K, Zhu H, Lei Y-L, He S, Yang J (2023) Dynamic characteristics of non-uniform multi-span functionally graded 3d graphene foams reinforced beams with elastic restraints. Composite Structures 321:117296
47. Gao K, Huang H, Zou Z, Wu Z, Zhu H, Yang J (2023) Buckling analysis of multi-span non-uniform beams with functionally graded graphene-reinforced foams, International Journal of Mechanical Sciences 108777
48. Gibson LJ, Ashby MF (1982) The mechanics of three-dimensional cellular materials, Proceedings of the Royal Society of London. Series A, Mathematical and Physical Sciences 382 (1782) 43–59
49. Pukhov GE (1978) Computational structure for solving differential equations by Taylor transformations. Cybernetics and Systems Analysis 14(3):383–390
50. Pukhov GE (1980) Differential Transformations of Functions and Equations. Naukova Dumka, Kiev
51. Pukhov GE (1982) Differential Analysis of Circuits. Naukova Dumka, Kiev
52. Pukhov GE (1986) Differential Transformations and Mathematical Modeling of Physical Processes. Naukova Dumka, Kiev
53. Bervillier C (2012) Status of the differential transformation method. Applied Mathematics and Computation 218(20):10158–10170

54. Mehne S. Hashemi (2022) Differential transform method: A comprehensive review and analysis, Iranian Journal of Numerical Analysis and Optimization 12 (3) 629–657
55. Narayana M, Shekar M, Siddheshwar P, Anuraj N (2021) On the differential transform method of solving boundary eigenvalue problems: An illustration. ZAMM - Journal of Applied Mathematics and Mechanics / Zeitschrift für Angewandte Mathematik und Mechanik 101(5):e202000114
56. Xie L-J, Zhou C-L, Xu S (2016) An effective numerical method to solve a class of nonlinear singular boundary value problems using improved differential transform method. SpringerPlus 5:1066
57. Hołubowski R, Jarczewska K (2017) The combination of multi-step differential transformation method and finite element method in vibration analysis of non-prismatic beam. International Journal of Applied Mechanics 09(01):1750010
58. Bekiryazici MM Zafer, Kesemen T (2021) Modification of the random differential transformation method and its applications to compartmental models, Communications in Statistics - Theory and Methods 50 (18) 4271–4292
59. MATLAB, version: 9.1.0 (R2016b), The MathWorks Inc., Natick, Massachusetts, United States, 2016. https://www.mathworks.com
60. Smith M (2014) ABAQUS/Standard User's Manual, Version 6.14, Dassault Systèmes Simulia Corp, United States
61. Burlayenko VN, Altenbach H, Dimitrova SD (2021) A material model-based finite element free vibration analysis of one-, two- and three-dimensional axially FGM beams, in: 2021 IEEE 2nd KhPI Week on Advanced Technology (KhPIWeek), pp. 628–633
62. Burlayenko V, Kouhia R, Dimitrova S (2024) One-dimensional vs. three-dimensional models in free vibration analysis of axially functionally graded beams with non-uniform cross-sections. Mechanics Composite Materials 60(1):1–20 **(in press)**